The Astrophysical Journal, 911:32 (13pp), 2021 April 10 https://doi.org/10.3847/1538-4357/abe705

Research on Multiwavelength Isolated Bright Points Based on Deep Learning

Li Xu[1], Yunfei Yang[1,2,5], Yihua Yan[2,3], Yin Zhang[2], Xianyong Bai[2], Bo Liang[1], Wei Dai[1], Song Feng[1], and Wenda Cao[4]
[1] Faculty of Information Engineering and Automation/Yunnan Key Laboratory of Computer Technology Application, Kunming University of Science and Technology, Kunming 650500, Yunnan, People's Republic of China; yangyf@kust.edu.cn
[2] CAS Key Laboratory of Solar Activity, National Astronomical Observatories, Beijing 100012, People's Republic of China
[3] School of Astronomy and Space Science, University of Chinese Academy of Sciences, Beijing 100049, People's Republic of China
[4] Big Bear Solar Observatory, New Jersey Institute of Technology, 40386 North Shore Lane, Big Bear City, CA 92314-9672, USA
Received 2020 October 16; revised 2021 February 15; accepted 2021 February 15; published 2021 April 13

Abstract

Multiwavelength bright points (BPs) are taken to be cross sections of magnetic flux tubes extending from the surface of the photosphere upward to the higher photosphere. We aim to study the characteristics of isolated multiwavelength BPs using the cotemporal and cospatial TiO band and Hα line wings from the Goode Solar Telescope at Big Bear Solar Observatory. A deep-learning method, based on Track Region-based Convolutional Neural Networks, is proposed to detect, segment, and match the BPs across multiple wavelength observations, including the TiO, H$\alpha+1$ Å, H$\alpha-1$ Å, H$\alpha+0.8$ Å, and H$\alpha-0.8$ Å line wings. Based on the efficient detection and matching result with a precision of 0.98, 1283 groups of BPs matched in all five wavelengths are selected for statistics analysis. The characteristic values of the BPs observed at the same red and blue line wings are averaged. For the BPs of the TiO, averaged H$\alpha\pm1$ Å, and averaged H$\alpha\pm0.8$ Å line wings, the mean equivalent diameters are 162 ± 32, 254 ± 33, and 284 ± 28 km, respectively. The maximum intensity contrasts are 1.11 ± 0.09, 1.05 ± 0.03, and $1.05\pm0.02\langle I_{QS}\rangle$, respectively. The mean eccentricities are 0.65 ± 0.14, 0.63 ± 0.11, and 0.65 ± 0.11, respectively. Moreover, the characteristic ratios of each H$\alpha\pm1$ Å and H$\alpha\pm0.8$ Å BP to its corresponding TiO BP are derived. H$\alpha\pm1$ Å and H$\alpha\pm0.8$ Å line wings BPs show 60% and 80% increases compared to TiO BPs, respectively. With increasing height, most BPs almost keep their shapes. This work is helpful for modeling the three-dimensional structure of flux tubes.

Unified Astronomy Thesaurus concepts: Quiet sun (1322); Solar photosphere (1518); Astronomical methods (1043); Convolutional neural networks (1938)

1. Introduction

Magnetic field lines are advected by photospheric granular convection into tight bundles to form thin flux tubes in the narrow dark intergranular lanes (Peckover & Weiss 1978; Stenflo 1985; Solanki 1993). These thin flux tubes rise from the depth of the solar convection zone to the solar surface, and expand with increasing height in the solar atmosphere (Jess et al. 2010a; Ji et al. 2012). They are thought to be the transport channels of energy for heating the solar corona, either via kinetic and Alfvén waves, or via magnetic reconnection (Roberts & Soward 1983; Parker 1988; Choudhuri et al. 1993; Müller et al. 2000; Berger & Title 2001; Rutten et al. 2001; Steiner et al. 2001; Schüssler et al. 2003; Ishikawa et al. 2007; de Wijn et al. 2009; Jess et al. 2009; Zhao et al. 2009; Balmaceda et al. 2010; Ji et al. 2012).

Owing to the increasing high-resolution observational technologies, several wavelengths can observe small-scale bright points (BPs) in the lower solar atmosphere, e.g., the photospheric surface by the TiO band (7057 Å), *G* band (4305 Å) and CN band (3880 Å), and the low chromosphere (or higher photosphere) by the Ca II H (3968 Å) wavelength and Hα line wings (6563 ± 1 Å), etc. The photospheric BPs are located within intergranular lanes ubiquitously, the majority of them having counterparts in the cotemporal and cospatial multiwavelength lower solar atmospheric observations. Although the line formation heights are very difficult to evaluate, reference can be provided according to the approximate depths where the various continua and lines originate, e.g., the line formation heights indicated by Vernazza et al. (1981). The height of the TiO band formation is estimated to be slightly higher than the *G* band. Different line positions in a scan of Hα will represent different heights in the lower solar atmosphere, ranging from the chromosphere at the core of the line to the photosphere at the line wings. The farther off-center the Hα line wing is, the closer it is to the photosphere. Therefore, these multiwavelength BPs appearing simultaneously in different wavelengths or line wings represent the cross sections of magnetic flux tubes at different heights in the lower solar atmosphere (Dunn & Zirker 1973; Mehltretter 1974; Solanki 1993). It is a good way to know more about the nature of thin flux tubes in three-dimensional (3D) space by exploring the characteristics of multiwavelength BPs.

The *G* band (4305 Å) and TiO band (7058 Å) are very suitable for observing the BPs on the photospheric surface, because they are dominated by absorption bands of temperature-sensitive molecules (Muller & Roudier 1984; Berger et al. 1995, 2007; Zakharov et al. 2005; Utz et al. 2009). The *G*-band BPs and TiO BPs appear visibly bright with clear edges, so they are easily detected. They are generally classified into isolated BPs and nonisolated ones. The isolated BPs represent the BPs that do not merge with other BPs or split into several BPs during their lifetimes, while the nonisolated ones are opposite. In terms of morphology, the isolated BPs appear in point-like shapes and the nonisolated ones in elongated chains, knees, or flowers (Dunn & Zirker 1973; Roudier et al. 1994; Berger et al. 1995; Müller et al. 2000; Sánchez Almeida 2004; Wiehr et al. 2004; Möstl et al. 2006; Ishikawa et al. 2007; Jess et al. 2009; Abramenko et al. 2010; Sánchez

[5] Corresponding author.

Almeida et al. 2010; Keys et al. 2011; Muller et al. 2011; Feng et al. 2013; Yang et al. 2015a, 2019; Ji et al. 2016; Xiong et al. 2017; Liu et al. 2018a). In terms of physics, the isolated BPs may represent single thin flux tubes, and the nonisolated ones may represent the concentration of several thin flux tubes (Requerey et al. 2015). Although the statistics come from the data obtained by the different telescopes with different diffraction limits and seeing, the quantification of isolated BPs on the photospheric surface has been well known by now. The typical equivalent diameter is ∼160 km, ranging from 70 to 400 km. The maximum intensity contrast is $\sim 1.1\langle I_{\rm QS}\rangle$, ranging from 0.7 to $1.9\langle I_{\rm QS}\rangle$ ($\langle I_{\rm QS}\rangle$ is the mean intensity of a quiet region where the BPs are embedded). The lifetime is several minutes. The horizontal velocity is 1 km s^{-1} ranging from 0 to 7 km s^{-1}.

The lower chromospheric Ca BPs are indiscernible because the bright Ca BPs are located within the bright intergranular lanes. Some investigations of Ca BPs were published, e.g., the mean diameter of ∼200 km, the maximum intensity contrast of $\sim 1.4\langle I_{\rm QS}\rangle$, etc. (Jess et al. 2010b; Jafarzadeh et al. 2013; Keys et al. 2013; Xiong et al. 2017). Some research paid attention to the photospheric BPs and the corresponding chromospheric BPs owing to the high-cadence multiwavelength observations in recent years. Jess et al. (2010a) reported that the intensity of *G*-band BPs and Ca II K BPs presents a power-law trend of the magnetic flux density. They also noted that field strengths affect the expansion of the flux tubes, with weak fields (50 G) leading to an expansion of ∼70%, whereas higher field strengths (150 G) lead to an expansion of ∼40%. Keys et al. (2013) also reported that Ca II K BPs are larger than *G*-band BPs by ∼60%. Xiong et al. (2017) estimated the mean ratio of the equivalent diameter for each Ca BP to its corresponding *G*-band BP as 1.2. Liu et al. (2018a) calculated the horizontal displacement from the centroid of a Ca II H BP to that of its corresponding *G*-band BP, and used the difference of the horizontal displacements between two consecutive frames to describe the change in the flux tube shape. They speculated that it might be caused by MHD waves propagating along the flux tubes.

There are some automatic detection methods that have been proposed in previous studies. The detection methods of BPs in the TiO and *G* band are compatible due to the similar features of BPs in these two bands. These methods adopt typical image technologies, such as threshold, region-growing algorithm, and mathematical morphology (Sánchez Almeida 2004; Bovelet & Wiehr 2007; Utz et al. 2009; Abramenko et al. 2010; Aniđić et al. 2010; Crockett et al. 2010; Muller et al. 2011; Xiong et al. 2017; Liu et al. 2018a, 2018b). Recently, Yang et al. (2019) used a deep-learning method, Mask RCNN, to detect and classify the *G*-band BPs into three types by their morphologies. On the other hand, the detection methods of Ca BPs are mainly manual or semiautomatic, which depend strongly on the spatial correspondence of *G*-band BPs (Riethmüller et al. 2010; Jafarzadeh et al. 2013; Keys et al. 2013; Liu et al. 2018a). Xiong et al. (2017) proposed a 3D tracking with detection method, which needs several steps to preprocess the Ca II H images, such as a white top-hat transform and black top-hat transform.

BPs can be seen in Hα line wings whose offset is beyond 0.6 Å from the line core. Goode et al. (2010) showed single BPs located at vertices of intergranular lanes in Hα − 1.25 Å quiet-Sun data. Yurchyshyn et al. (2010) indicated that BPs seen in different line positions in a scan of Hα images are very well correlated with the Ca II H BPs, which in turn are cospatial with *G*-band BPs. However, the quantitative studies of Hα line wing BPs are rarely reported. There is no existing automatic detection method for detecting BPs in the Hα line wings, and no automatic matching method for matching the photospheric BPs and the Hα line wings BPs. In this paper, a new deep-learning method, Track Region-based Convolutional Neural Networks (Track-RCNN), is used to detect, segment, and match the isolated BPs in the five lines of TiO (λ7058 Å), Hα (λ6563 Å) + 1 Å, Hα − 1 Å, Hα + 0.8 Å, and Hα − 0.8 Å simultaneously. Based on the effective detection and matching results with a precision of 0.98, we performed statistical analysis on the characteristics of the isolated BPs that matched in all five lines, in terms of area, equivalent diameter, intensity contrast, and eccentricity. This study will fill the gap of the characteristic statistics of isolated BPs at Hα line wings and the correlation with TiO BPs. It will enrich our knowledge of the 3D structures of thin flux tubes extending from the surface of the photosphere to the higher photosphere.

The paper is organized as follows. The data, including the data sets and how to build the data sets, are described in detail in Section 2. The methods including training and testing the deep-learning network are detailed in Section 3. Section 4 details the detection and matching results, and the statistical results of the multiwavelength BPs that matched in all five lines. The evaluation of the method is also briefly presented in Section 4. Section 5 discusses the method and the statistical results. Finally, the conclusion is given in Section 6.

2. Data

2.1. Data Sets

Goode Solar Telescope (GST) at the Big Bear Solar Observatory (BBSO) is an off-axis 1.6 m clear aperture telescope that offers unprecedented high spatial resolution and polarimetric capabilities (Cao et al. 2010; Goode & Cao 2012). The AO-308-equipped GST has achieved nearly diffraction-limited observations at a spatial resolution below 0.″1, which is ideal for the study of small-scale physical processes in the photosphere and chromosphere. The imaging observations of the photosphere are performed with Broadband Filter Imager by using a broadband TiO filter centered at a wavelength of 705.7 nm. The Visible Imaging Spectrometer is a Fabry–Pérot-interferometer-based tunable filter system that performs imaging spectroscopy in Hα.

The data adopted in this work comprise the image series of five cospatial and cotemporal wavelengths, including the TiO band (7058.0 Å), Hα (6563 Å) + 1 Å, Hα − 1 Å, Hα + 0.8 Å, and Hα − 0.8 Å line wings. All raw images were corrected for dark current and flat field, and speckle-reconstructed employing the KISIP speckle reconstruction code (Wöger et al. 2008). Hereafter, the group of cospatial and cotemporal TiO, Hα + 1 Å, Hα − 1 Å, Hα + 0.8 Å, and Hα − 0.8 Å image series is referred to as the group of TiO-Hα image series. The interval of each group of TiO-Hα image series is lower than 30 s. Note that the Hα data from BBSO/GST includes 11 wavelengths. Only four wavelengths whose offset is beyond H$\alpha \pm 0.6$ Å were adopted because the offset within ±0.6 Å are relatively far away from the photosphere, and no BPs can be seen in that line wings.

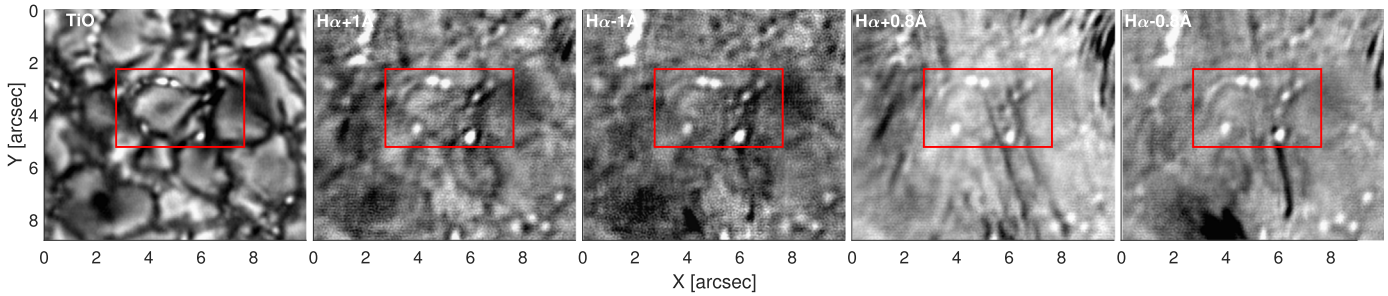

Figure 1. Group of cospatial and cotemporal images of TiO, Hα + 1 Å, Hα − 1 Å, Hα + 0.8 Å, and Hα − 0.8 Å observed on 2019 August 10. The TiO image was observed at 17:11:39 UT, and the corresponding Hα observations were several seconds earlier or later. The subregions with the red boxes will be detailed in Figure 4.

Table 1
The Parameters of the Data Set

Data Set	Date	Time Period (UT)	Region	FOV[a] Size ($'' \times ''$)	Pixel Size TiO, ($''$)	Pixel Size Hα, ($''$)	Frames	Purpose
D1	2014-08-05	16:51:28–17:22:21	*nearAR*	2×2	0.0375	0.0356	972×5	Training set
D2	2019-08-10	17:03:39–21:48:29	*QR*	14.5×14.5	0.0375	0.0290	152×5	Testing set/statistical analysis

Note.
[a] Field of view.

Figure 1 shows a group of TiO-Hα image series, which were obtained from GST on 2019 August 10. The TiO image was observed at 17:11:39 UT, and the corresponding Hα observations were several seconds earlier or later. It can be seen that the TiO BPs are obviously visible with sharp edges, which are located in the dark intergranular lanes; the Hα BPs that are offset by ± 1 Å from the center are nearly visible with clear structure; the Hα BPs offset by ± 0.8 Å are barely visible with blurred edges. We also found that the BPs in the different Hα line wing images almost correspond spatially to TiO BPs.

The deep-learning method needs data sets for training and testing the networks. Therefore, building the data sets is the first step. Table 1 lists the data we used to build the data sets. Two image series observed in 2014 and 2019 were used to build the training set and test set separately. Due to unstable seeing in those times, we selected relatively good-quality images from them. Data set 1 (D1) is the training set for training the network. The images were obtained near an active region at the center of the solar disk. From them, we selected small subregions with a size of $2'' \times 2''$ to build samples of the training set. The subregions were selected representatively, in which there are several isolated BPs with various shapes or different surroundings. The small size of the subregions is to improve the training speed under the limited memory. The training set consists of a total of 972 groups of TiO-Hα image series (corresponding 972×5 frames), for which 80% of the samples were used for training and 20% for validating during training. Data set 2 (D2) was obtained in a quiet-Sun region, which is also close to the solar disk center. Its aim is to build the testing set and statistical analysis. Among them, five groups of representative TiO-Hα image series were selected to build the testing set, which is to test and confirm the actual power of the network.

2.2. Building Data Sets

The TiO-Hα image series were carefully aligned by a high-accuracy registration algorithm that is based on a cross-correlation technique (Yang et al. 2015b) in which the alignment accuracy reaches the subpixel level. The displacement between the TiO and cotemporal Hα + 1 Å images is obtained by this alignment method, and then the other Hα images are shifted according to the displacement.

The images contain a periodic pattern and salt-and-pepper noise due to unstable seeing in the observation period. Therefore, we used notch filtering to reduce the periodic pattern and nonlocal mean filtering to reduce the salt-and-pepper noise separately. The notch filter (also known as reject filter) is defined as a device that rejects or blocks the transmission of frequencies within a specific frequency range and allows frequencies outside that range (Hong et al. 2010). The nonlocal mean filtering is not a local smoothing method. Instead, the pixels of the image that have a high similarity of image blocks are weighted-averaged to denoise (Buades et al. 2005). For the Hα images, notch filtering with the frequency domain radius at 30 Hz was performed first. After that, we used the nonlocal average filtering with the parameters nwr as 1, swr as 3, and h as 2, where nwr is the radius of the neighborhood window, swr is the radius of the search window, and h is the smoothing parameter of the Gaussian function. Due to the relatively good quality of the TiO band, only the nonlocal average filtering with the parameters including nwr as 1, swr as 1, and h as 1 was performed. Figure 1 shows the five wavelength images after reducing the periodic pattern.

After denoising, we performed equidistant intensity normalization for the TiO-Hα image series in both the training and testing sets. Its aim is to improve the similarity of BPs in the different wavelengths, so that the deep-learning method can simultaneously detect multiwavelength BPs in the TiO-Hα image series. The intensities of the TiO-Hα image series are normalized from 0 to 255 first. The second step is performing the equidistant intensity level threshold from maximum intensity to zero intensity for images (Bovelet & Wiehr 2007; Crockett et al. 2009). It yields a pattern of cells surrounding each local intensity maximum. After repeated experiments, we set the thresholds to 20 for the TiO, 18 for the H$\alpha \pm 1$ Å, and 16 for the H$\alpha \pm 0.8$ Å images, respectively. The relatively small threshold is suitable for the BPs with blurred edges in the

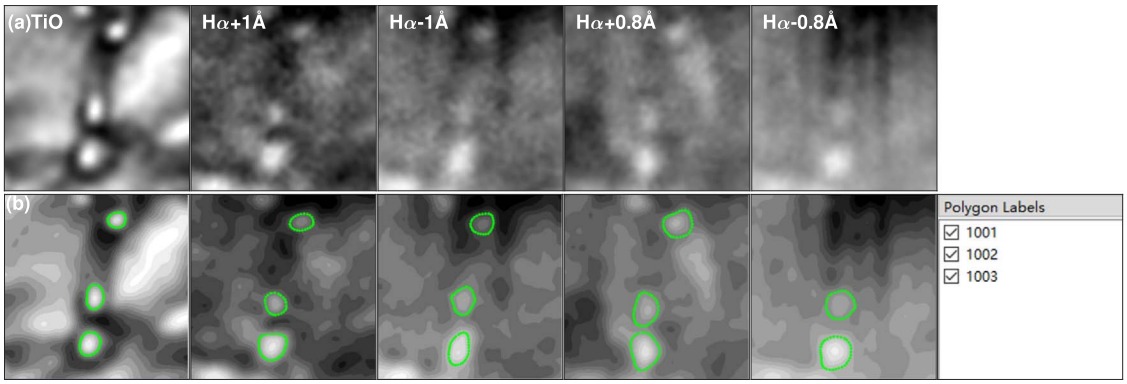

Figure 2. Screenshots of the LabelMe tool in use. The multiwavelength BPs are polygons annotated by clicking along their boundaries, and are given labels. (a) The original images of the TiO-Hα image series; (b) the preprocessed TiO-Hα image series with their labeled BPs and labels.

H$\alpha \pm 0.8$ Å images. The last step is normalizing the intensities of all pixels in each cell to the average intensity of the cell. Figure 2(b) shows the images after equidistant intensity normalization.

The LabelMe tool (Russell et al. 2008) was used to build the data sets referring to the multitarget tracking data set (Geiger et al. 2012; Voigtlaender et al. 2019). The cospatial and cotemporal isolated BPs in the equidistant intensity normalized TiO-Hα image series are polygons annotated by clicking along their boundaries and are given the corresponding labels for detection, segmentation, and matching. To conveniently describe the cospatial and cotemporal isolated BPs across the TiO-Hα image series, hereafter we call them the group of multiwavelength BPs. Note that a group of multiwavelength BPs may appear in some or several of the multiwavelength images, not always in all five multiwavelength images. Figure 2 shows a labeling example. It can be seen that the isolated BP has a core cell, for which the intensity is significantly greater than its surrounding cells. Note that if two close-by BPs have two clear core cells and their own surrounding cells, they will be taken as samples and given the labels. If not, they will not be labeled as samples. In Figure 2(b), three groups of multiwavelength BPs are labeled in a set of TiO-Hα image series, of which two groups cross all five wavelength images separately, and one group only has four BPs because there is no counterpart that can be seen in H$\alpha - 0.8$ Å image. The first number of the label is class_id, which represents the class of the group. All labeled BPs belong to the same class in this work. The next numbers are track_id, which represents the tracking order in the set of images. A group of multiwavelength BPs has the same label.

The above steps were performed in both training and testing sets, but there are a few differences between them. Only certain BPs are selected to build the training set, most of which have counterparts in more than three wavelength images. However, the BPs in the images of the testing set are labeled as ground truths as much as possible, even if they only have one counterpart. The ground truth refers to the accuracy of the testing set. As a result, a total of 7937 BPs in different wavelength images, which form 1879 groups of multiwavelength BPs, are labeled in the training set. A total of 1617 BPs, which form 611 groups, are labeled as ground truths in the testing set.[6]

3. Methods

3.1. Detection, Segmentation, and Matching

We adopted a deep-learning method, Track-RCNN[7] (Voigtlaender et al. 2019), to detect and segment the multiwavelength BPs in the TiO-Hα image series, and to match the corresponding BPs jointly with a neural network. There are three main parts: detection, segmentation, and matching. The aim of detection is to locate the BPs with bounding boxes. Segmentation is to find the masks of BPs in the pixel level. Matching is to associate the multiwavelength BPs that belong to the same flux tube. Note that the matching task is based on the tracking module of Track-RCNN. Track-RCNN provides mask-based detections together with association features, which are inputted to a tracking algorithm that decides which detections to select and how to link them over time with temporal dynamics. By referring to the idea of tracking, multiwavelength BPs can be associated over a multiwavelength dimension for matching, instead of the time dimensional of tracking. The structure (or flow) of the method is shown in Figure 3, mainly including the backbone, 3D convolutions layers, Region Proposal Network (RPN), bounding-box regression, classification, mask generation, association, and Hungarian matching.

The deep-learning method needs to train the network first. The following are the main steps of training for the multiwavelength BPs.

D1 is inputted into the backbone, ResNet50 (He et al. 2016), which includes four residual blocks consisting of 50 convolutional layers and max pooling layers. A total of 1024 feature maps are then obtained.

The feature maps are passed to two depth-separable 3D convolution layers with $3 \times 3 \times 3$ filter kernels. It augments the feature maps with the contexts in the multiwavelength dimension. A total of 1024 enhanced features are obtained.

The enhanced features are then passed to the RPN (Ren et al. 2015). The RPN is a fully convolutional network, which is trained to generate detection proposals with various scales and aspect ratios by using a sliding window. Each proposal is a rectangle with a score for measuring object class.

The proposals are fed into two sibling fully connected layers, a bounding-box regression layer, and a classification layer. The detection results, including classification label, bounding box,

[6] The data sets are available at http://61.166.157.71/Multiwavelength-BP-Track-RCNN.html.

[7] The codes are available at https://github.com/VisualComputingInstitute/TrackR-CNN.

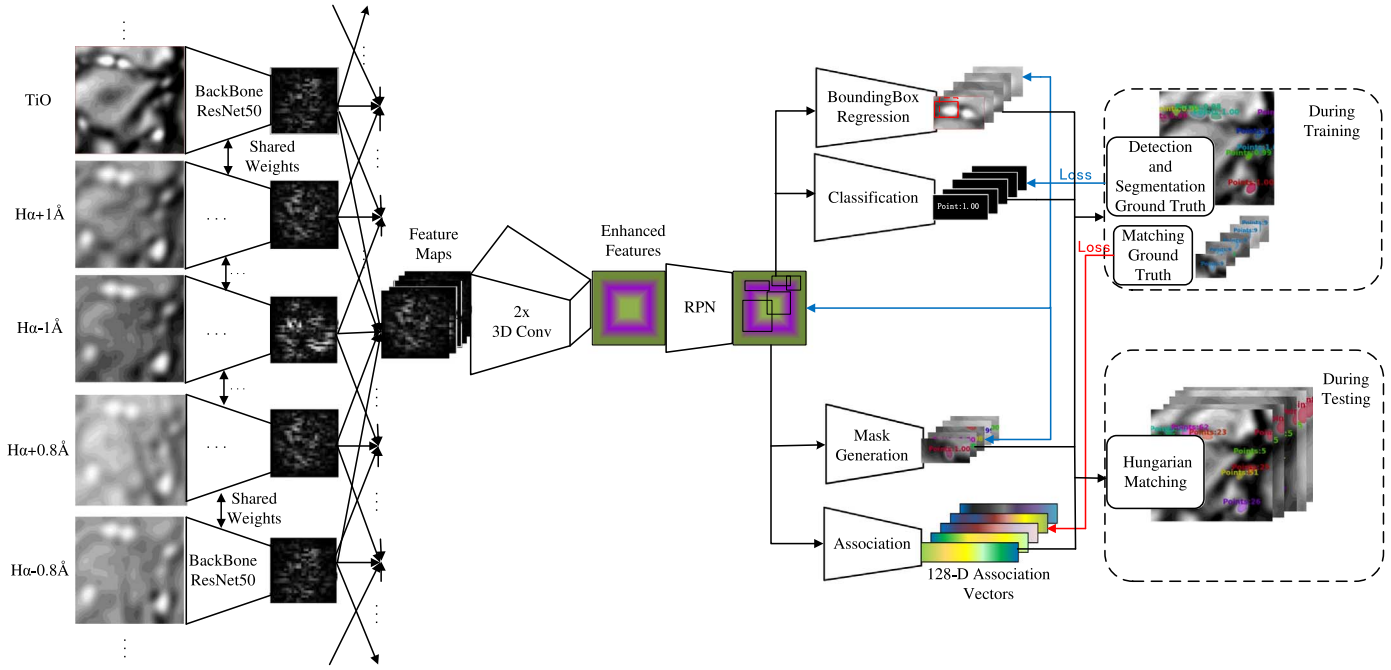

Figure 3. Structure (or flow) of the method including three main parts: detection, segmentation, and tracking.

and confidence score, for each detected BP are achieved after the redundant boxes are eliminated by Non-Maximum Suppression (NMS; Neubeck & Gool 2006). The NMS is to suppress elements that are not maximum values, which can be positively formulated as a local maximum search, where a local maximum is greater than all of its neighbors. Meanwhile, the masks of the BPs are generated based on the mask generation network, for which the prediction for each pixel in the upsampled last feature map obtained by the deconvolution layer is generated by a full convolutional network (Long et al. 2015; He et al. 2017). The loss function is designed for detecting and masking as a multitask loss, $L = L_{\rm cls} + L_{\rm box} + L_{\rm mask}$, where $L_{\rm cls}$ is classification loss, $L_{\rm box}$ is bounding-box loss, and $L_{\rm mask}$ is mask loss (Ren et al. 2015; He et al. 2017).

The detection results are fed into the association, which is a fully connected layer that predicts an association vector for each proposal. They are trained in a way that vectors belonging to the same instance are close to each other and vectors belonging to different instances are far away from each other. We define the distance $d(v, w)$ between two association vectors v and w as their Euclidean distance, $d(v, w) := \|v - w\|$. The association network is trained by using the batch-hard triplet loss proposed by Voigtlaender et al. (2017). This loss samples positives and negatives for each detection. Formally, let D denote the set of detections. Each detection $d \in D$ consists of a mask, mask_d, and an association vector, a_d, which comes from frame f_d and is assigned a ground-truth track ID, id_d, determined by its overlap with the ground-truth objects. The association loss in the batch-hard formulation with margin α is then given by

$$\frac{1}{|D|}\sum_{d\in\mathcal{D}} \max\left(\max_{\substack{e\in\mathcal{D}\\ id_e=id_d}} \|a_e - a_d\| - \min_{\substack{i\in\mathcal{D}\\ id_e\neq id_d}} \|a_e - a_d\| + \alpha, 0\right). \quad (1)$$

Training a network is to adjust the parameters of each layer by executing the feed-forward propagation and back propagation in iterations. The propagation algorithm includes a series of operations such as convolution and pooling, calculating the classification probability, bounding box, and mask, etc., and then the loss value of the loss function is fed back to the entire network by the back-propagation algorithm, that is, the gradient of each layer is calculated using the Adam optimizer to continuously adjust the weight of each parameter to minimize the loss. The training procedure is iterated until the loss value converges steadily.

After training the network, the TiO-Hα image series with any size can be fed to the trained network. The feed-forward propagation is performed only once with the flow of Figure 3, except for back propagation with loss functions. The similarity feature matrix between any two detected BPs is calculated by their association vectors obtained through the association network. Besides that, the Euclidean distance matrix between any two BPs detected by their bounding boxes centers is calculated. The BPs are then matched by the Hungarian matching algorithm (Kuhn 1955), which takes the feature similarity and limited distance into account according to these two matrices. The Hungarian matching algorithm is the most common algorithm for bipartite graph matching. The core of the algorithm is to find the augmented path, which is an algorithm to find the maximum matching of the bipartite graph by using the augmented path.

Finally, the Hα BPs that only appear in one Hα line wing are excluded. All detected TiO BPs are reserved due to their relatively sharp edges and clear structures.

3.2. Training and Testing

We deployed the programs on a personal computer with a single GTX2080 GPU (8 GB device RAM). The platform comprises Python 3 and TensorFlow 1.8, including some packages, such as pycocotools, numpy, sklearn, pypng, opencv-python, munkres, cython, scikit-image, pillow,

Table 2
The Testing Metrics

Metrics	TiO	Hα + 1 Å	Hα − 1 Å	Hα + 0.8 Å	Hα − 0.8 Å	Mean
Precision	0.92	0.89	0.85	0.81	0.87	0.87
Recall	0.98	0.95	0.93	0.94	0.94	0.95
AP	0.92	0.86	0.81	0.77	0.83	0.84
*F*1	0.95	0.91	0.89	0.87	0.90	0.90

matplotlib, and scipy. The training set was fed to train the network. After repeated experiments, the hyperparameters of the network was fine-tuned in order to fit small-scale multiwavelength BPs, e.g., Optimizer as Adam, LEARNING_RATE as 5×10^{-7}, anchor_sizes as (2, 4, 8, 16, 32), anchor_ratios as (0.5, 1, 2), FASTRCNN_NMS_THRESH as 0.75, FASTRCNN_FG_RATIO as 0.25, and Batch_size as 3. The loss value converges steadily for 50,000 iterations, which cost about 30 hr. On average, it takes about 2 s on each iteration. We called the trained network Multiwavelength-BP-Track-RCNN.[8]

The testing set, consisting of 611 groups of multiwavelength BPs, were fed to Multiwavelength-BP-Track-RCNN to evaluate the power of the network. We used four metrics—precision, recall, AP, and *F*1-score—to evaluate the detection results thoroughly. For detailed descriptions of precision, recall, and AP, please see Yang et al. (2019). The *F*1-score is another metric which also takes into account both precision and recall, just like AP. It is regarded as a weighted average of the precision and recall (Fernandez-Moral et al. 2018).

Table 2 lists the four metrics evaluated for the test set. The mean precision, recall, AP, and *F*1-score are 0.87, 0.95, 0.84, and 0.9, respectively. The highest precision belongs to the TiO BPs and the lowest belongs to Hα + 0.8 Å. There is no obvious difference in recall values. The TiO BPs has the best AP value, 0.92, which is a good score. The corresponding *F*1-scores are all higher than that of AP values. Both of them have similar evaluation results. Note that, they are not ideal metrics for comparisons between different facilities and data sets, but we hope they can provide some reference for future works on similar data sets or facilities.

Based on the metrics satisfied by the method, D2, consisting of 152 groups of TiO-Hα image series, was fed to Multiwavelength-BP-Track-RCNN. As a result, a total of 44,783 isolated BPs are detected, segmented, and matched. It takes about 5 s for each image on average. In order to quantify the multiwavelength BPs, a total of 6415 BPs, corresponding to 1283 groups of multiwavelength BPs that matched in all five wavelengths, were reserved to do statistical analysis.

4. Results

4.1. Instances

Figure 4 shows the detection and matching procedures of the regions marked by red boxes in Figure 1. The original multiwavelength images (a), the detected multiwavelength BPs (b), the matched multiwavelength BPs (c), and the multiwavelength BPs that only matched in all five wavelengths (d) are displayed from top to bottom. The images from left to right are presented in each row in the order of TiO, Hα + 1 Å, Hα − 1 Å, Hα + 0.8 Å, and Hα − 0.8 Å, respectively.

In Figure 4(b), all detected isolated multiwavelength BPs are highlighted in various shades of red, which have high-confidence scores that are greater than 0.9. The missed BPs are circled in yellow, and the false detected points are in green. All isolated TiO BPs are detected correctly. A total of six Hα + 1 Å BPs are detected correctly, with a missed BP and a false detected point. In the Hα − 1 Å line wing, there are seven BPs correctly detected but one error. In the Hα + 0.8 Å line wing, there are six corrected, one missed, and two errors. On the other hand, all seven Hα − 0.8 Å BPs are correctly detected.

Figure 4(c) shows the matched multiwavelength BPs after excluding the Hα BPs that only appear in one Hα line wing. The corresponding multiwavelength BPs are highlighted in the same color with the same ID. For instance, the BP with ID 23 represents a common type of thin flux tubes, whose size shown in the Hα ± 1 Å line wing is larger than that in the TiO band, and that in the Hα ± 0.8 Å line wing is larger than that in the Hα ± 1 Å line wing. On the other hand, the BPs with IDs 25, 32, and 44 (circled in red) are clearly visible in the TiO band, but they are difficult to detect at the corresponding positions in the Hα line wings. The BP with ID 26 is matched in three wavelengths, although it is missed in the Hα + 1 Å and Hα + 0.8 Å line wings.

Figure 4(d) shows the multiwavelength BPs that matched in all five lines. In order to further explore the characteristics of the matched multiwavelength BPs, we quantified areas, equivalent diameters, maximum intensity contrasts, and eccentricities of the multiwavelength BPs in Figure 4(d). These characteristics are defined below.

The area of a BP refers to the square kilometers corresponding to the actual pixel area occupied. The equivalent diameter is defined as $\mathrm{sqrt}(4S/\pi)$, where S represents the area. The maximum intensity contrast is defined as the ratio of the peak intensity of a BP to the average intensity of its embedded quiet field of view. The shape of a BP is represented by its eccentricity. It is the ratio of the distance between the foci of the ellipse and its major axis length, which for an ellipse can be any number from 0 (the limiting case of a circle) to arbitrarily close to but less than 1 (elongated ellipse).

Table 3 lists the above characteristics of the matched multiwavelength BPs in Figure 4(d). The BPs with IDs 5, 8, 9, 23, and 51 conform to the phenomenon that BPs expand with height, increasing from the photosphere to the higher photosphere. However, the area of the Hα − 1 Å BP with ID 62 is smaller than its corresponding TiO BP. It is also smaller than those of the corresponding BPs in the other Hα line wings. All multiwavelength BPs are slightly brighter than the quiet Sun. The maximum intensity contrasts of most TiO BPs are larger than those of Hα BPs. For the eccentricities of the matched multiwavelength BPs, there is no trend, just like they appear in different shapes in Figure 4.

4.2. Statistics

4.2.1. Characteristics of Multiwavelength BPs

Precision is more important than recall for ensuring the reliability of the statistical analysis. It is good that the precision is high, up to 0.98 for the 1283 groups of multiwavelength BPs that matched in all five wavelengths. Based on the effective

[8] The trained network, Multiwavelength-BP-Track-RCNN, is available at http://61.166.157.71/Multiwavelength-BP-Track-RCNN.html.

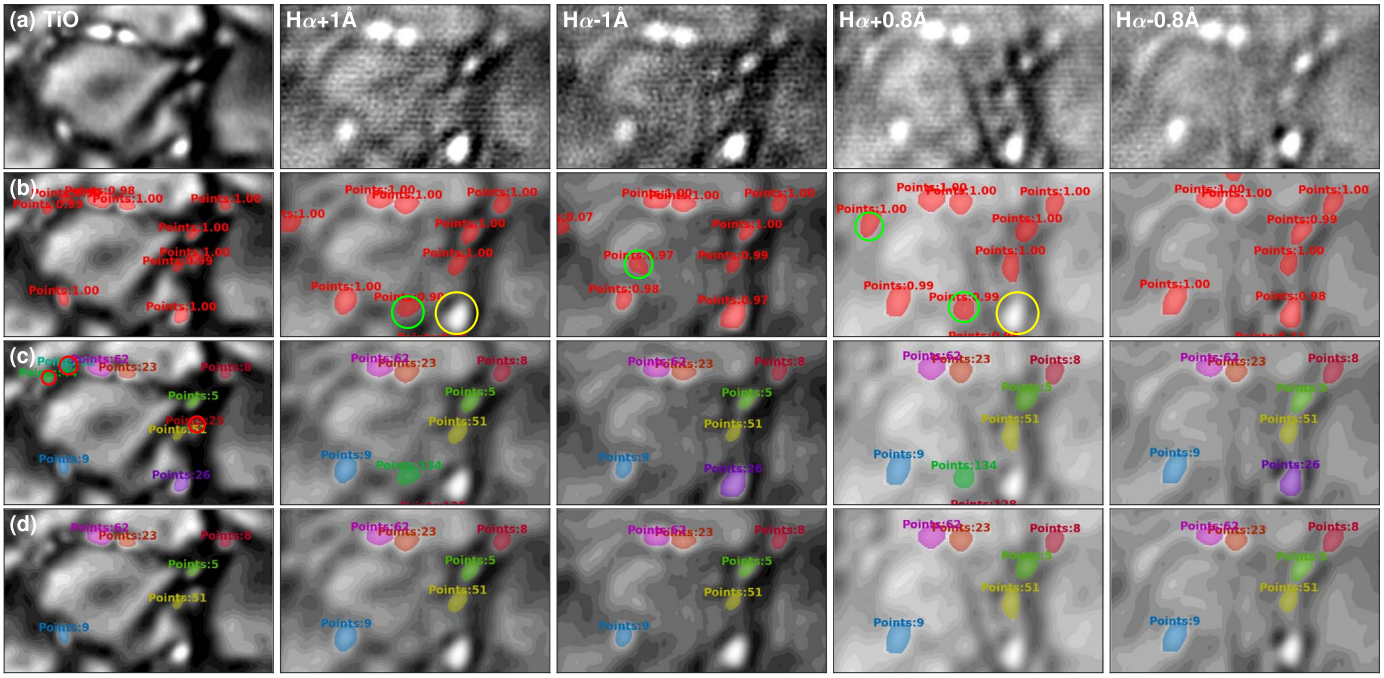

Figure 4. Detection and matching procedures of the regions marked by red boxes in Figure 1. The multiwavelength images (a), the detected multiwavelength BPs (b), the matched multiwavelength BPs (c), and the multiwavelength BPs that only matched in all five wavelengths (d) are displayed from top to bottom. The images from left to right are presented in each row in the order of TiO, Hα + 1 Å, Hα − 1 Å, Hα + 0.8 Å, and Hα − 0.8 Å, respectively. The missed BPs are circled in yellow and the false detected ones are in green.

Table 3
The Characteristics of Multiwavelength BPs in Figure 4(d)

ID	Characteristics	TiO	Hα + 1 Å	Hα − 1 Å	Hα + 0.8 Å	Hα − 0.8 Å
5	Area (km^2)	16,024	42,852	430,194	68,616	64,186
5	Equivalent diameter (km)	143	234	196	296	286
5	Intensity contrast ($\langle I_{QS}\rangle$)	1.07	1.03	1.03	1.02	1.05
5	Eccentricity	0.79	0.78	0.79	0.63	0.81
8	Area (km^2)	16,449	45,990	36,576	57,488	64,423
8	Equivalent diameter (km)	145	242	216	271	286
8	Intensity contrast ($\langle I_{QS}\rangle$)	1.07	1.02	1.02	1.04	1.03
8	Eccentricity	0.22	0.69	0.69	0.71	0.75
9	Area (km^2)	22,047	79,006	43,669	101,447	94,986
9	Equivalent diameter (km)	167	317	236	359	348
9	Intensity contrast ($\langle I_{QS}\rangle$)	1.13	1.05	1.03	1.07	1.06
9	Eccentricity	0.72	0.66	0.68	0.73	0.78
23	Area (km^2)	24,196	59,782	53,611	67,825	56,327
23	Equivalent diameter (km)	175	276	261	294	268
23	Intensity contrast ($\langle I_{QS}\rangle$)	1.29	1.07	1.04	1.07	1.06
23	Eccentricity	0.78	0.68	0.77	0.29	0.46
51	Area (km^2)	14,220	50,236	30,458	70,936	54,429
51	Equivalent diameter (km)	134	253	197	301	263
51	Intensity contrast ($\langle I_{QS}\rangle$)	1.00	1.02	1.01	1.03	1.02
51	Eccentricity	0.75	0.80	0.78	0.83	0.73
62	Area (km^2)	57,172	63,473	42,016	82,829	64,449
62	Equivalent diameter (km)	269	284	231	325	286
62	Intensity contrast ($\langle I_{QS}\rangle$)	1.31	1.07	1.04	1.09	1.07
62	Eccentricity	0.74	0.75	0.64	0.58	0.73

detection and matching results, these BPs are adopted for statistical analysis.

Figure 5 shows the histograms of the multiwavelength BP characteristics (blue dashed line) and the best-fit curves (red solid line) in terms of area, equivalent diameter, maximum intensity contrast, and eccentricity, respectively. Based on previous studies (Utz et al. 2009; Feng et al. 2013; Yang et al. 2015a, 2019; Ji et al. 2016; Xiong et al. 2017; Liu et al.

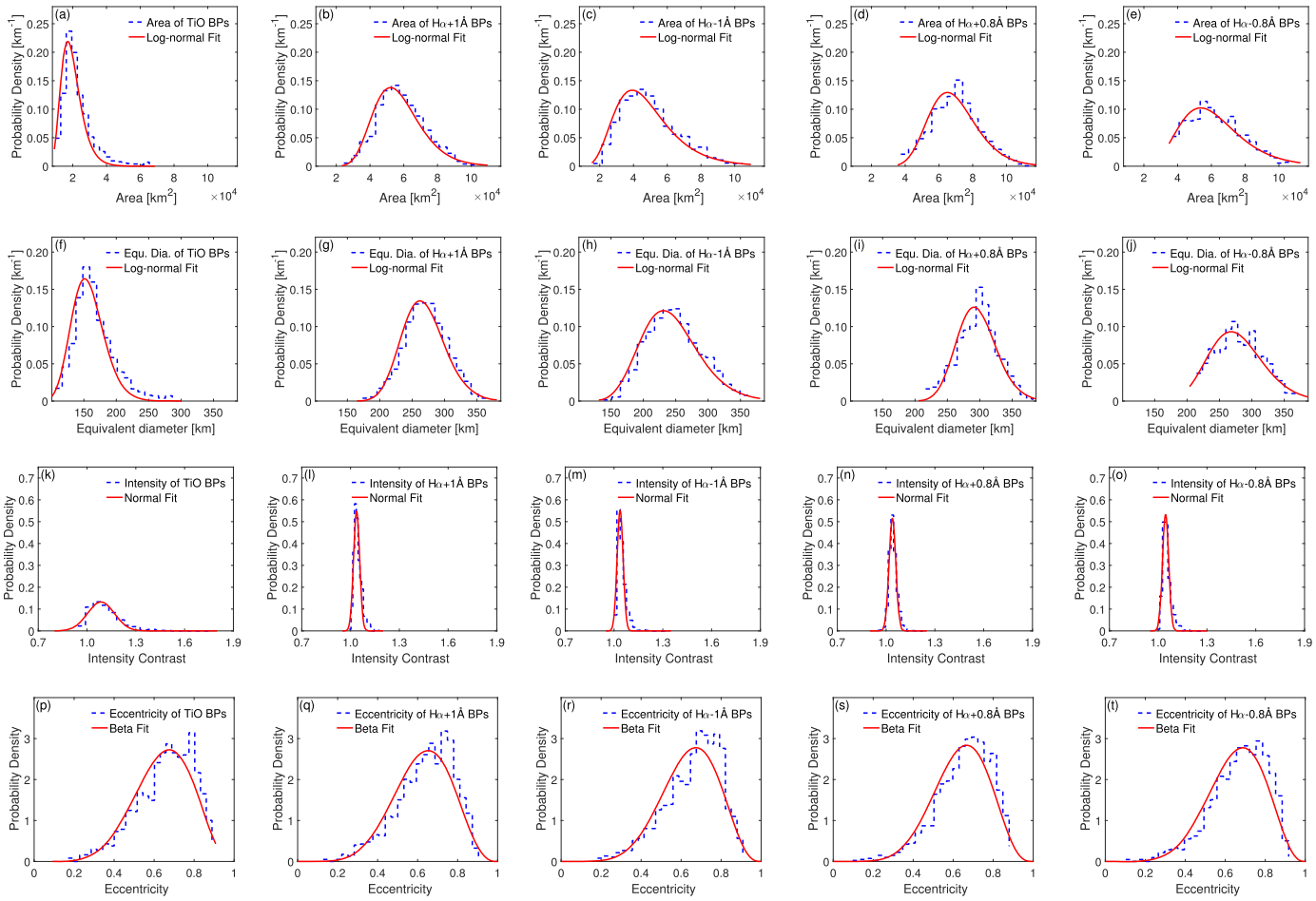

Figure 5. Histograms of the multiwavelength BP characteristics (blue dashed line), and the best-fit curves (red solid line). The first row: the area histograms and their log-normal distributions for the TiO band (a), Hα + 1 Å line wing (b), Hα − 1 Å line wing (c), Hα + 0.8 Å line wing (d), and Hα − 0.8 Å line wing (e), respectively. The second row: the equivalent diameter histograms and fitted curves following log-normal distributions for the TiO band (f), Hα + 1 Å line wing (g), Hα − 1 Å line wing (h), Hα + 0.8 Å line wing (i), and Hα − 0.8 Å line wing (j), respectively. The third row: the maximum intensity contrast histograms and fitted curves following normal distributions for the TiO band (k), Hα + 1 Å line (l), Hα − 1 Å line wing (m), Hα + 0.8 Å line wing (n), and Hα − 0.8 Å line wing (o), respectively. The fourth row: the eccentricity histograms and fitted curves following Beta distributions for the TiO band (p), Hα + 1 Å line wing (q), Hα − 1 Å line wing (r), Hα + 0.8 Å line wing (s), and Hα − 0.8 Å line wing (t), respectively.

Table 4
The Characteristics of the Multiwavelength BPs Matched in Five Lines

Characteristics	TiO	Hα + 1 Å	Hα − 1 Å	Averaged H$\alpha \pm 1$ Å	Hα + 0.8 Å	Hα − 0.8 Å	Averaged H$\alpha \pm 0.8$ Å
Area (km^2)	$21{,}459 \pm 9165$	$56{,}276 \pm 3940$	$47{,}511 \pm 16841$	$51{,}894 \pm 13450$	$67{,}536 \pm 14271$	$61{,}162 \pm 15658$	$64{,}349 \pm 12654$
[*min*, *max*]	[*7959, 67015*]	[*22125, 106827*]	[*13607, 106958*]	[*19843, 99218*]	[*35125, 117532*]	[*34677, 109490*]	[*35336, 111244*]
Equivalent diameter (km)	162 ± 32	266 ± 33	242 ± 43	254 ± 33	292 ± 31	277 ± 35	284 ± 28
[*min, max*]	[*100, 292*]	[*167, 369*]	[*131, 369*]	[*157, 355*]	[*211, 387*]	[*210, 373*]	[*212, 376*]
Intensity contrast ($\langle I_{QS} \rangle$)	1.11 ± 0.09	1.05 ± 0.03	1.05 ± 0.03	1.05 ± 0.03	1.04 ± 0.03	1.05 ± 0.03	1.05 ± 0.02
[*min, max*]	[*0.94, 1.80*]	[*0.99, 1.19*]	[*0.99, 1.35*]	[*0.99, 1.27*]	[*0.95, 1.24*]	[*0.99, 1.29*]	[*0.99, 1.21*]
Eccentricity	0.65 ± 0.14	0.63 ± 0.14	0.65 ± 0.14	0.63 ± 0.12	0.64 ± 0.14	0.66 ± 0.14	0.65 ± 0.11
[*min, max*]	[*0.15, 0.90*]	[*0.11, 0.92*]	[*0.16, 0.92*]	[*0.15, 0.89*]	[*0.08, 0.90*]	[*0.08, 0.93*]	[*0.26, 0.87*]

2018a, 2018b), we selected the most suitable fitting curve to fit the histogram. Table 4 lists the quantization of the characteristics corresponding to Figure 5.

As shown in Figures 5(a)–(e), the area histograms of the corresponding multiwavelength BPs are well fitted by the log-normal function. The area distribution of the TiO BPs is relatively narrow and steep, while those of the others become wider and flatter. The mean areas and standard deviations of TiO BPs, Hα + 1 Å BPs, Hα − 1 Å BPs, Hα + 0.8 Å BPs, and Hα − 0.8 Å BPs are $(2.15 \pm 0.92) \times 10^4$, $(5.63 \pm 1.39) \times 10^4$, $(4.75 \pm 1.68) \times 10^4$, $(6.75 \pm 1.43) \times 10^4$, and $(6.12 \pm 1.57) \times 10^4$ km^2, respectively. Figures 5(f)–(j) show the equivalent diameter histograms and their log-normal distributions. The equivalent diameters of TiO BPs, Hα +

Table 5
The Ratios of the Corresponding Hα BPs and TiO BPs

Characteristics	Hα + 1 Å	Hα − 1 Å	Averaged Hα ± 1 Å	Hα + 0.8 Å	Hα − 0.8 Å	Averaged Hα ± 0.8 Å
Equivalent diameter (ratio)	1.68 ± 0.31	1.53 ± 0.32	1.60 ± 0.29	1.85 ± 0.34	1.76 ± 0.34	1.80 ± 0.32
[*min, max*]	[*0.86, 2.95*]	[*0.69, 2.96*]	[*0.78, 2.78*]	[*0.96, 3.24*]	[*0.80, 3.08*]	[*0.96, 3.08*]
Eccentricity (ratio)	1.03 ± 0.38	1.05 ± 0.36	1.04 ± 0.35	1.05 ± 0.39	1.07 ± 0.39	1.07 ± 0.39
[*min,max*]	[*0.23, 3.38*]	[*0.25, 3.80*]	[*0.27, 3.53*]	[*0.12, 3.73*]	[*0.15, 3.78*]	[*0.32, 3.39*]

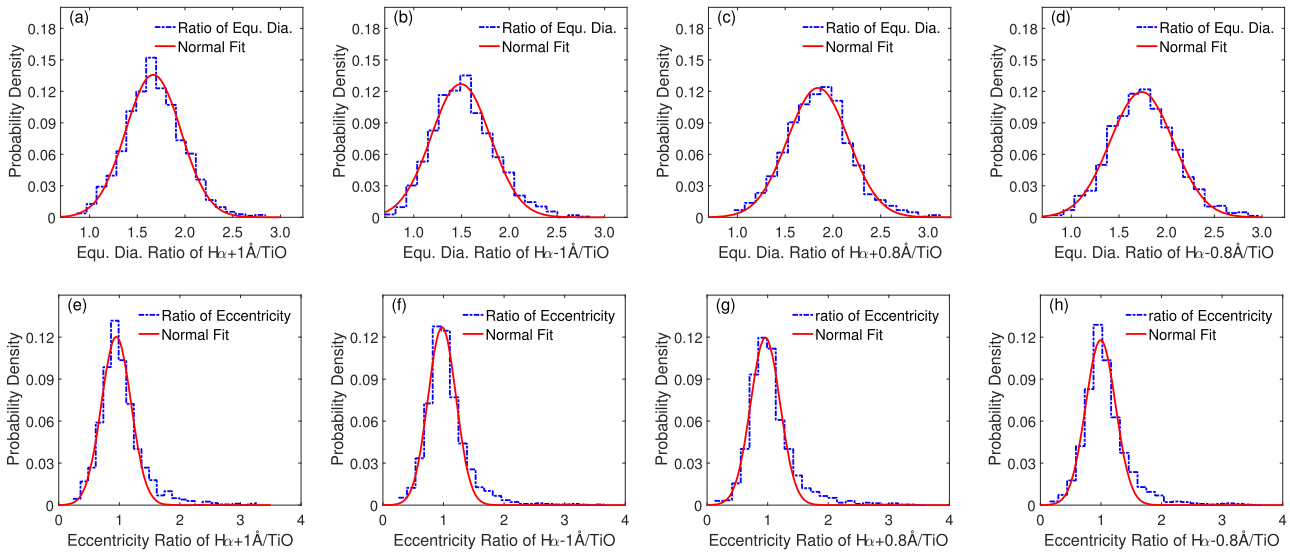

Figure 6. Histograms (blue dashed–dotted line) and the best-fit functions (red solid line) of the ratios of the corresponding Hα BPs and TiO BPs in terms of equivalent diameter (a)–(d) and eccentricity (e)–(h), respectively.

1 Å BPs, Hα − 1 Å BPs, Hα + 0.8 Å BPs, and Hα − 0.8 Å BPs are 162 ± 32, 266 ± 33, 242 ± 43, 292 ± 31, and 277 ± 35 km, respectively. There is a clear trend that the sizes of the Hα + 0.8 Å BPs and Hα −0.8 Å BPs are slightly enhanced compared to those of Hα + 1 Å BPs and Hα − 1 Å BPs, and the sizes of the Hα + 1 Å BPs and Hα − 1 Å BPs are larger than those of TiO BPs.

As seen in Figures 5(k)–(o), the maximum intensity contrasts of the multiwavelength BPs are densely distributed in the value of 1, which follow the normal distributions well. The distribution of TiO BPs is relatively wide, with a mean value of $1.11\langle I_{QS}\rangle$ ranging from 0.94 to $1.80\langle I_{QS}\rangle$. On the other hands, the BPs of the Hα + 1 Å, Hα − 1 Å, Hα + 0.8 Å, and Hα − 0.8 Å line wings have fairly narrow and steep distribution curves. They are in mean intensity contrast of 1.05 ± 0.03, 1.05 ± 0.03, 1.04 ± 0.03, and $1.05 \pm 0.03\langle I_{QS}\rangle$, for which the mean values are very similar. The maximum values of all Hα BPs are lower than 1.4. The majority of multiwavelength BPs are slightly brighter than their surroundings.

Figures 5(p)–(t) show the eccentricity histograms and the Beta curves. There is no significant difference in the distributions of the multiwavelength BPs. All of them are flat and wide curves, which means the BPs have various shapes. The mean values are about 0.64 ± 0.14, ranging from ∼0.1 to ∼0.9. There is no multiwavelength BP with a standard circle shape. Most of them tend to be elliptical, probably because they are squeezed within the narrow dark intergranular lanes by the granular convection. The BPs with the largest eccentricity value are elongated ellipses that have a core cell. Note that this work cannot exclude the chains of BPs that have a bright central region.

We averaged the values of each pair of multiwavelength BPs at the same Hα line wings to reflect the cross sections of the flux tubes at the average height of the symmetrical red and blue line wings, such as the values of Hα + 1 Å BP and Hα − 1 Å BP, and Hα + 0.8 Å BP and Hα − 0.8 Å BP. As much as possible, the offset between the positions of the narrowing filter at the symmetrical red and blue line wings can be ignored. The distributions of these characteristics are not plotted here because they are very similar to those of Figure 5. The averaged values of Hα ± 1 Å and Hα ± 0.8 Å are listed in Table 5. The averaged equivalent diameters of Hα ± 1 Å and Hα ± 0.8 Å BPs are 254 ± 33 and 284 ± 28 km, respectively. These values can better reflect the cross section of the thin flux tubes at the corresponding heights of Hα ± 1 Å and Hα ± 0.8 Å respectively. The intensity contrasts and eccentricities of the same line wings are very close, so the averaged values are not surprising.

4.2.2. Ratios of Characteristics

In order to further quantify the various behaviors of each magnetic flux tube from the surface of the photosphere to the higher photosphere, we calculated the characteristic ratios of each Hα BP to its corresponding TiO BP in terms of equivalent diameter and eccentricity. Note that the intensity contrast of BPs is mainly due to the filters the observations are performed with; therefore, the ratio for intensity is not discussed here. Figure 6 shows the histograms of the ratios of the Hα + 1 Å, Hα − 1 Å, Hα + 0.8 Å, Hα − 0.8 Å BPs to their corresponding TiO BPs (blue dashed–dotted line) and their fitted curves that all follow a normal distribution function (red solid line). Table 5 lists the corresponding ratio values. We also

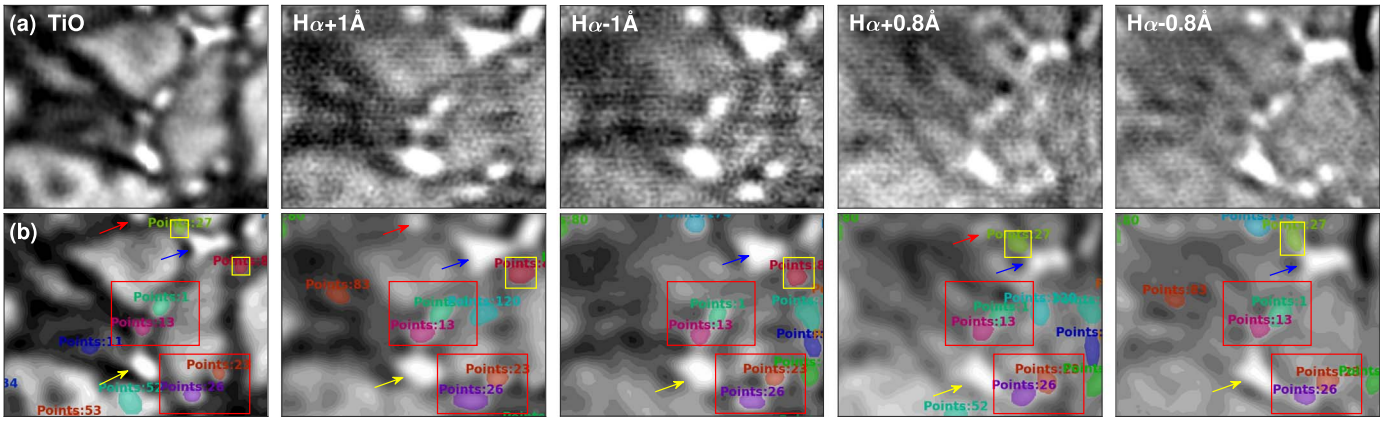

Figure 7. Detection and matching results of a corresponding TiO-Hα region observed at 18:44:10 UT (the observation time of TiO band) on 2019 August 10; (a) the multiwavelength images; (b) the detection and matching results. All of the BPs with colors are detected correctly. Some objects (with arrows) that look like BPs are not detected.

calculated the ratios of the averaged characteristics of the BPs at the same line wings to their corresponding TiO BPs. All the mean values are listed in Table 5.

Figures 6(a)–(d) show the distributions of the equivalent diameter ratios. All distributions of the equivalent diameter ratios are flat and wide. Most equivalent diameter ratio values are larger than 1. That means the size of most Hα BPs is larger than that of corresponding TiO BPs. There are very few ratio values lower than 1 shown in the distribution, which is not more than 1%. That means the size of such Hα BP is smaller than that of corresponding TiO BPs. The mean values and the standard deviations are 1.68 ± 0.31 for H$\alpha + 1$ Å, 1.53 ± 0.32 for H$\alpha - 1$ Å, 1.85 ± 0.34 for H$\alpha + 0.8$ Å, and 1.76 ± 0.34 for H$\alpha - 0.8$ Å. The quantification implies that the majority of BPs expand from the surface of the photosphere (TiO band) upward to the higher photosphere (Hα line wings), with an approximate expansion of ~0.6 to the height corresponding to the H$\alpha \pm 1$ Å line wing, and ~0.8 corresponding to the H$\alpha \pm 0.8$ Å line wing.

As shown in Figures 6(e)–(h), the fitted curves of the eccentricity ratios of Hα BPs to their corresponding TiO BPs follow normal distributions very well. They are all evenly dispersed around the ratio of 1. If the ratio value is close to 1, it means that the BP almost keeps its shape. If the ratio is lower than 1, the BP changes to become rounded. Otherwise, the BP changes to become elongated. The average ratios of the eccentricity of corresponding Hα BPs and TiO BPs are very similar, with the mean ratio of 1.03 ± 0.36. That means with the BPs extending from the photosphere to the lower chromosphere, most of them almost keep their shapes, and the others change their shapes randomly.

5. Discussion

5.1. Multiwavelength-BP-Track-RCNN

In order to know more about the cross sections of flux tubes at the different heights at the lower solar atmosphere, we present a deep-learning method, based on Track-RCNN, to simultaneously detect, segment, and match the multiwavelength BPs at five observation lines, including the TiO band, H$\alpha + 1$ Å, H$\alpha - 1$ Å, H$\alpha + 0.8$ Å, and H$\alpha - 0.8$ Å line wings.

Previous works detected BPs mainly according to their intensities and intensity gradients (Sánchez Almeida 2004; Bovelet & Wiehr 2007; Utz et al. 2009; Abramenko et al. 2010; Aniđić et al. 2010; Crockett et al. 2010; Muller et al. 2011; Xiong et al. 2017; Liu et al. 2018a, 2018b). Our method mainly depends on the feature extraction by deep learning. The deep-learning networks can extract and fuse the BPs' distinct features in different levels, angles, scales, and even the embedded backgrounds after the parameters of the networks are fine-tuned during training. In terms of matching, the previous works matched the multiwavelength BPs in the photosphere and the lower chromosphere mainly according to the spatial location (de Wijn et al. 2005; Guglielmino et al. 2010; Riethmüller et al. 2010; Jafarzadeh et al. 2013; Keys et al. 2013; Xiong et al. 2017; Liu et al. 2018a). For instance, Xiong et al. (2017) matched the *G*-band BPs and Ca II H BPs by the nearest neighbor strategy. This kind of matching method can easily cause a mismatch if the BPs have other close neighbors. However, our method matches the multiwavelength BPs using the Hungarian algorithm according to two matrices. One is a similarity feature matrix between any two detected BPs, which is derived by their association vectors obtained through the association network. Another is a Euclidean distance matrix between any two detected BPs, which is calculated using the centers of their bounding boxes. This strategy associates the BPs depending on feature similarity and limited distance together, therefore effectively solving the above problem.

Figure 7 shows a detection and matching example of a group of TiO-Hα regions observed at 18:44:10 UT (the observation time of TiO band) on 2019 August 10. It can be seen that all BPs with colors are detected correctly. Some objects (with arrows) that look like BPs are not picked up by the method. In detail, the objects with a red arrow are incomplete because they are at the edge of the images; the objects with a blue arrow are nonisolated BPs; and the objects with a yellow arrow are difficult to judge whether they are big BPs, two merging BPs, or exploding granules. In terms of matching, the matched BPs marked by red boxes even have close neighbors—they are matched correctly. Besides that, the BPs with yellow boxes that are only detected in some of the line wings are also matched effectively. Our method overcomes difficulties such as confused surroundings, vague edges, and close neighbors in some ways.

Our method, as well as previous methods, detects the multiwavelength BPs first, and then matches them. The

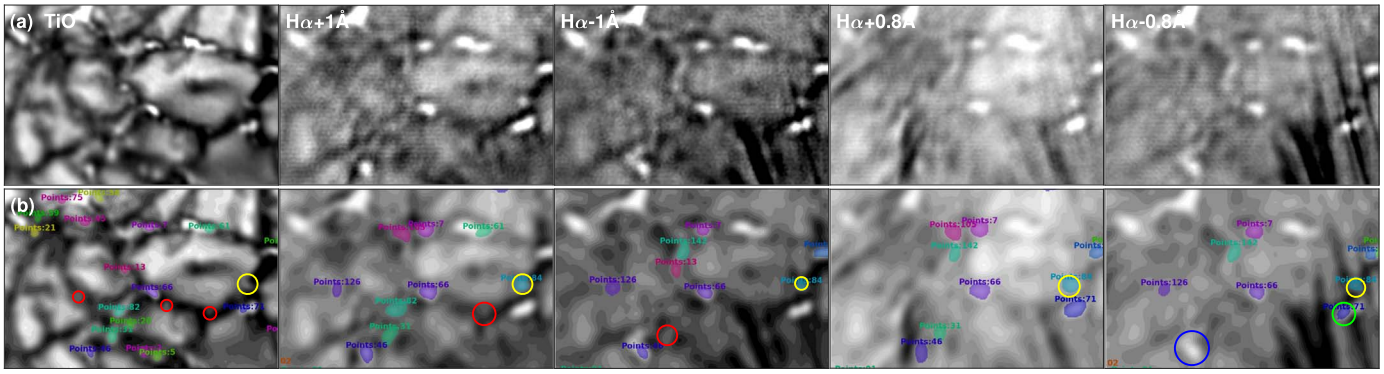

Figure 8. Some cases that are only detected in some of the line wings. The detection and matching results of a corresponding TiO-Hα region observed at 17:14:39 UT (the observation time of TiO band) on 2019 August 10; (a) the multiwavelength images; (b) the detection and matching results. The BPs circled in red that looks like a BP fail to be picked up, for they are too weak to have a clear intensity gradient. Another BP circled in blue is caused by a confused edge that fuses with other features. The BPs with yellow circles are not clearly visible in the TiO band or fuse with the adjacent granule, but are clearly visible in the Hα line wings.

matching results depend on the detection results strongly. We checked the matched multiwavelength BPs carefully, especially those BPs that are only detected in some of line wings. Figure 8 shows some typical cases. For instance, the BPs circled in red that look like BPs fail to be picked up, for they are too weak to have a clear intensity gradient. Another BP circled in blue is caused by a confused edge which fuses with other features. We also found that a few BPs, e.g., the BPs with yellow circles, are not clearly visible in the TiO band or fuse with the adjacent granule, but are clearly visible in the Hα line wings. Note that the BP circled in green in the Hα $-$ 0.8 Å line wing is over features like rapid blueshifted excursions (RBEs). Whether it is detected depends on how it is cut off by RBEs or rapid redshifted excursions (RREs). If it still remains a relatively complete shape, it will be detected. However, there is something that needs to be improved. The boundaries of some segmented BPs are not perfect, e.g., the BPs with IDs 23 and 62 in Figure 4 have smaller mask edges. One possible reason is caused by equidistant intensity normalization, whose equidistant intensity level threshold affects the boundary of BPs. Another possible reason is that the mask generation network of the method, which often predicts labels on a low-resolution regular grid after downsampling, should be mostly smooth, i.e., neighboring pixels often take the same label. A regular grid will unnecessarily oversample the smooth areas while simultaneously undersampling object boundaries. The result is blurry contours as a compromise between undersampling and oversampling (see Figure 1 in Kirillov et al. 2020). We have checked the detection results of D2; most BPs have reasonable edges. This will not trouble the statistics results based on a large amount of data.

5.2. Characteristics of Multiwavelength BPs

In order to explore the characteristics of the thin flux tubes extending from the surface of the photosphere (TiO band) upward to the higher photosphere (Hα line wings), 1283 groups of multiwavelength BPs that matched in all five lines are statistical analyzed. The statistical results show that (1) the majority of BPs expand with an approximate expansion rate of $\sim$1.6 to the height corresponding to the H$\alpha \pm 1$ Å line wing, and $\sim$1.8 corresponding to the H$\alpha \pm 0.8$ Å line wing; (2) the BPs have various shapes. Extending up, most BPs almost retain their shapes, and the others change their shapes randomly; (3) the majority of BPs are a little brighter than their embedded regions.

In terms of the equivalent diameter of TiO BPs, the mean equivalent diameter and the standard deviation is 162 ± 32 km with a range of 100–292 km. Aniđić et al. (2011) proposed that the mean diameter of the TiO BPs observed from GST is 166 km. Abramenko et al. (2010) revealed that the diameters of TiO BPs range from 77 to 260 km, whose data also come from GST. Our results are consistent with them. Besides that, Ji et al. (2016) analyzed the TiO BPs in six regions with different magnetic levels observed from the NVST. They provide the mean equivalent diameters of TiO BPs ranging from 168 to 195 km, for which the smaller the magnetic levels of the embedded region are, the smaller the size of the TiO BP is. Liu et al. (2018b) derived a mean diameter for the isolated TiO BPs of 163 km also using the data from NVST. This means that the diameter of TiO BPs are accepted to be $\sim$160 km, even though the data come from different telescopes. Our minimum value of 100 km is larger than that of Abramenko et al. (2010). The main reason is that the statistics only comes from the BPs matched in all five observed lines, which causes the weak and small TiO BPs to be excluded.

The mean equivalent diameters are 266 ± 33 km for the Hα $+$ 1 Å line wing, 242 ± 43 km for the Hα $-$ 1 Å line wing, 292 ± 31 km for the Hα $+$ 0.8 Å line wing, and 277 ± 35 km for the Hα $-$ 0.8 Å line wing, respectively. The mean size of the BPs of the red line wings is slightly superior to that of blue wing BPs. The reason why they have different sizes is possibly caused by the small offset between the distances of the filter from the line core of the red and blue wings. Therefore, we averaged the values of each pair of multiwavelength BPs at the same Hα line wings. The mean equivalent diameter of the H$\alpha \pm 1$ Å line wing is 254 ± 33 km, while that of the H$\alpha \pm 0.8$ Å line wing is 284 ± 28 km. BPs show a $\sim$60% increase up to the H$\alpha \pm 1$ Å line wing and $\sim$80% to the H$\alpha \pm 0.8$ Å line wing. Previous studies published the expansion rates of BPs extending from the photosphere to lower chromospheres. Jess et al. (2010a) found an expansion of 76% in area between *G*-band BPs and Na_ID_1 BPs at the lowest magnetic flux densities (50 G). Keys et al. (2013) revealed the corresponding average sizes of 51,800 for Ca II K BPs and 31,300 km^2 for *G*-band BPs, which show an average increase of 65% from the photosphere to the chromosphere. Then, Xiong et al. (2017) obtained an equivalent diameter ratio of 1.2 using the data from the *G* band and Ca II *H* band. Comparing

them, we got a higher expansion rate of ∼60% in diameter upward to Hα ± 1 Å line wings, and ∼80% upward to Hα ± 0.8 Å line wings. It is noted that the expansion of BPs as they extend upward is affected by many factors, such as, e.g., the line formation height, field strength, the extending distance, the angle of flux tubes, etc. (Jess et al. 2010a; Xiong et al. 2017). Not only that, the image quality should not be ignored, as Jess et al. (2010a) described the lower intensity contrasts of BPs look like a larger expansion. This might have caused the larger sizes of the Hα line wing BPs owing to the lower intensity contrast of the Hα images. So, we remind readers that the expansion ratios of BPs do not completely equal the real expansion of thin flux tubes.

In terms of the maximum intensity contrast, the mean value of the TiO BPs is $1.11\langle I_{QS}\rangle$ with a range from 0.94 to $1.80\langle I_{QS}\rangle$. The maximum intensity contrast of TiO BPs is about $1–1.3\langle I_{QS}\rangle$ with a range from 0.8 to $1.8\langle I_{QS}\rangle$ (Sánchez Almeida 2004; Möstl et al. 2006; Romano et al. 2012; Feng et al. 2013; Utz et al. 2013; Yang et al. 2014, 2019; Xiong et al. 2017; Liu et al. 2018b). Ji et al. (2016) found that the mean contrast values of TiO BPs observed from NVST range from 0.99 to $1.06\langle I_{QS}\rangle$, and the lowest value belongs to the weak magnetic field region. Liu et al. (2018b) revealed that the mean intensity contrast of the isolated TiO BPs is $1.08\langle I_{QS}\rangle$. Our results are in agreement with them. The intensity contrasts of Hα BPs are lower than those of TiO BPs. The intensity contrasts depend on the observation wavelength. TiO is a continuum filter that will have a higher intensity of light incident on the detector, which means that it is easier for the observer to reach higher count levels across the detector. Within the BPs, this is exacerbated as the higher temperature causes dissociation in some of the continuum lines, which gives a higher contrast for BPs. The Hα line will not have this effect (continuum dissociation). Also, as this is a line scan for Hα, the filter tends to be narrow at a given wavelength step to allow narrow tuning across the line, which will affect counts across the chip and subsequently the contrast ratios that are obtained at each wavelength step. This, coupled with a poorer relative image contrast with narrow filtering and possible Doppler shifting within the image pixels, will result in a more smeared-out feature that appears dimmer.

6. Conclusion

The multiwavelength BPs are taken as good tracers of the magnetic flux tubes at different heights in the lower solar atmosphere. It is a good way to know further about the magnetic thin flux tubes extending from the surface of the photosphere upward to the higher photosphere by detecting, segmenting, and matching the cotemporal and cospatial TiO BPs and Hα line wing BPs, and then measuring their characteristics.

We present a deep-learning method, Multiwavelength-BP-Track-RCNN, based on Track-RCNN architecture, to detect and match the multiwavelength BPs. Two data sets observed at five lines including the TiO band, Hα + 1 Å, Hα − 1 Å, Hα + 0.8 Å, and Hα − 0.8 Å line wings from BBSO/GST are used. The data observed on 2014 August 5 are used to build the training set. The data of 2019 August 10 are used to do statistical analysis, and some of them are used to build the testing set. After several steps of preprocessing, including alignment, the notch filtering and the nonlocal mean filtering, and equidistant intensity normalization, the training set including 1879 groups of multiwavelength BPs and the testing set including 611 groups of multiwavelength BPs are built. The Multiwavelength-BP-Track-RCNN, which mainly consists of ResNet50, 3D convolutions layers, RPN, bounding-box regression, classification, mask generation, association, and Hungarian matching, is trained on a personal computer with a GTX2080 GPU (8 GB device RAM). It requires 30 hr for training after executing 50,000 iterations until the loss value converges stably. Then, the testing set is fed to the trained Multiwavelength-BP-Track-RCNN, which takes about 5 s for each image on average. The method achieves efficient detection and matching of multiwavelength BPs with a precision of 0.87, recall of 0.95, AP of 0.84, and $F1$-score of 0.90. The training set and testing set come from different years and different regions. It also implies that the method is efficient and adaptable. As a result, a total of 44,783 isolated BPs are detected, segmented, and matched. Finally, a total of 6415 BPs that correspond to 1283 groups of multiwavelength BPs that are matched in all five wavelengths, with the precision high up to 0.98, are selected to do statistical analysis.

The mean area values of multiwavelength BPs at the TiO band, Hα + 1 Å, Hα − 1 Å, Hα + 0.8 Å, and Hα −0.8 Å line wings are $(2.15 \pm 0.92) \times 10^4$ km^2, $(5.63 \pm 1.39) \times 10^4$ km^2, $(4.75 \pm 1.68) \times 10^4$ km^2, $(6.75 \pm 1.43) \times 10^4$ km^2, and $(6.12 \pm 1.57) \times 10^4$ km^2, respectively. Then, the characteristics of each pair of BPs belonging to the same line wing are averaged, such as the Hα + 1 Å BP and Hα − 1 Å BP, and the Hα + 0.8 Å BP and Hα − 0.8 Å BP. The average area of the Hα ± 1 Å line wing is $(5.19 \pm 1.35) \times 10^4$ and $(6.44 \pm 1.27) \times 10^4$ km^2 of the Hα ± 0.8 Å line wing.

The mean equivalent diameters of multiwavelength BPs are 162 ± 32 km for the TiO band, 266 ± 33 km for Hα + 1 Å, 242 ± 43 km for Hα − 1 Å, 292 ± 31 km for Hα + 0.8 Å, and 277 ± 35 km for the Hα − 0.8 Å line wing, respectively. The mean value of Hα ± 1 Å is 254 ± 33 km, and that of Hα ± 0.8 Å is 284 ± 28 km. In order to further quantify the change of the magnetic flux tubes from the surface of the photosphere to the higher photosphere, we calculate the characteristic ratios of each Hα BP to its corresponding TiO BP. The mean equivalent diameter ratios of Hα ± 1 Å and Hα ± 0.8 Å are 1.60 ± 0.29 and 1.80 ± 0.32 separately. It indicates that TiO BPs show a 60% increase up to Hα ± 1 Å line wing and a 80% increase to Hα ± 0.8 Å line wing.

The maximum intensity contrasts of multiwavelength BPs are 1.11 ± 0.09, 1.05 ± 0.03, 1.05 ± 0.03, 1.04 ± 0.03, and $1.05 \pm 0.03\langle I_{QS}\rangle$, respectively. The mean intensity contrasts are 1.05 ± 0.03 for the Hα ± 1 Å line wing and $1.05 \pm 0.02\langle I_{QS}\rangle$ for the Hα ± 0.8 Å line wing, respectively. In terms of eccentricity, the mean values are very similar to the value of 0.65, and the ratios of eccentricities are 1.03 ± 0.38, 1.05 ± 0.36, 1.05 ± 0.39, and 1.07 ± 0.39, respectively.

The distributions and statistical results imply that the majority of the magnetic flux tubes expand with increasing height in the lower solar atmosphere. The cross sections of magnetic flux tubes have irregular shapes. Most of them almost retain their shapes with increasing height.

This research extends our knowledge of the characteristics of multiwavelength BPs in different Hα line wings and the correlation with TiO BPs. The statistical results provide a valuable reference to know what the thin flux tubes look like, and how they expand from the surface of the photosphere to the higher photosphere. It might be useful for modeling the 3D structures of magnetic flux tubes. In the future, we plan to track

multiwavelength BPs to explore the dynamics of the flux tubes in four dimensions, which consists of three space dimensions and a time dimension.

The authors thank the referees very much for their careful reading and constructive comments. The authors are grateful for the support received from the National Natural Science Foundation of China (Nos. 11763004, 11573012, 11803085, 12063003, 11729301, 11973057, U1931107) and the Open Research Program of the Key Laboratory of Solar Activity of the Chinese Academy of Sciences (Nos. KLSA202019). The authors are grateful to the BBSO teams. BBSO operation is supported by NJIT and US NSF AGS-1821294 grant. GST operation is partly supported by the Korea Astronomy and Space Science Institute, the Seoul National University, and the Key Laboratory of Solar Activities of Chinese Academy of Sciences (CAS) and the Operation, Maintenance, and Upgrading Fund of CAS for Astronomical Telescopes and Facility Instruments. This work is also supported by the National Key Research and Development Program of China (2018YFA0404603), Yunnan Key Research and Development Program (2018IA054), and Yunnan Applied Basic Research Project (2018FB103).

ORCID iDs

Yunfei Yang https://orcid.org/0000-0001-9927-7541
Xianyong Bai https://orcid.org/0000-0003-2686-9153

References

Abramenko, V., Yurchyshyn, V., Goode, P., & Kilcik, A. 2010, ApJL, 725, L101
Aniđić, A., Chae, J., Goode, P. R., et al. 2011, ApJ, 731, 29
Aniđić, A., Goode, P. R., Chae, J., et al. 2010, ApJL, 717, L79
Balmaceda, L., Vargas Domínguez, S., Palacios, J., Cabello, I., & Domingo, V. 2010, A&A, 513, L6
Berger, T. E., Rouppe van der Voort, L., & Löfdahl, M. 2007, ApJ, 661, 1272
Berger, T. E., Schrijver, C. J., Shine, R. A., et al. 1995, ApJ, 454, 531
Berger, T. E., & Title, A. M. 2001, ApJ, 553, 449
Bovelet, B., & Wiehr, E. 2007, SoPh, 243, 121
Buades, A., Coll, B., & Morel, J.-M. 2005, in IEEE Computer Society Conf. on Computer Vision and Pattern Recognition (CVPR'05) (Piscataway, NJ: IEEE), 60
Cao, W., Gorceix, N., Coulter, R., et al. 2010, AN, 331, 636
Choudhuri, A. R., Auffret, H., & Priest, E. R. 1993, SoPh, 143, 49
Crockett, P. J., Jess, D. B., Mathioudakis, M., & Keenan, F. P. 2009, MNRAS, 397, 1852
Crockett, P. J., Mathioudakis, M., Jess, D. B., et al. 2010, ApJL, 722, L188
de Wijn, A. G., Rutten, R. J., Haverkamp, E. M. W. P., & Sütterlin, P. 2005, A&A, 441, 1183
de Wijn, A. G., Stenflo, J. O., Solanki, S. K., & Tsuneta, S. 2009, SSRv, 144, 275
Dunn, R. B., & Zirker, J. B. 1973, SoPh, 33, 281
Feng, S., Deng, L., Yang, Y., & Ji, K. 2013, Ap&SS, 348, 17
Fernandez-Moral, E., Martins, R., Wolf, D., & Rives, P. 2018, in 2018 IEEE Intelligent Vehicles Symp. (IV) (Piscataway, NJ: IEEE), 1051
Geiger, T., Wellens, T., & Buchleitner, A. 2012, PhRvL, 109, 030601
Goode, P. R., & Cao, W. 2012, Proc. SPIE, 8444, 844403
Goode, P. R., Yurchyshyn, V., Cao, W., et al. 2010, ApJL, 714, L31
Guglielmino, S. L., Bellot Rubio, L. R., Zuccarello, F., et al. 2010, ApJ, 724, 1083
He, K., Gkioxari, G., Dollar, P., & Girshick, R. 2017, in IEEE Int. Conf. on Computer Vision (ICCV) (Piscataway, NJ: IEEE), 2980
He, K., Zhang, X., Ren, S., & Sun, J. 2016, in IEEE Conf. on Computer Vision and Pattern Recognition (CVPR) (Piscataway, NJ: IEEE), 770
Hong, X., Wang, D., Xu, L., & He, S. 2010, OExpr, 18, 12415
Ishikawa, R., Tsuneta, S., Kitakoshi, Y., et al. 2007, A&A, 472, 911
Jafarzadeh, S., Solanki, S. K., Feller, A., et al. 2013, A&A, 549, A116
Jess, D. B., Mathioudakis, M., Christian, D. J., Crockett, P. J., & Keenan, F. P. 2010a, ApJL, 719, L134
Jess, D. B., Mathioudakis, M., Christian, D. J., et al. 2010b, SoPh, 261, 363
Jess, D. B., Mathioudakis, M., Erdélyi, R., et al. 2009, Sci, 323, 1582
Ji, H., Cao, W., & Goode, P. R. 2012, ApJL, 750, L25
Ji, K.-F., Xiong, J.-P., Xiang, Y.-Y., et al. 2016, RAA, 16, 78
Keys, P. H., Mathioudakis, M., Jess, D. B., et al. 2011, ApJL, 740, L40
Keys, P. H., Mathioudakis, M., Jess, D. B., et al. 2013, MNRAS, 428, 3220
Kirillov, A., Wu, Y., He, K., & Girshick, R. B. 2020, in IEEE/CVF Conf. on Computer Vision and Pattern Recognition (CVPR) (Piscataway, NJ: IEEE), 9796
Kuhn, H. W. 1955, Naval Research Logistics Quarterly, 2, 83
Liu, Y., Wu, N., & Lin, J. 2018a, RAA, 18, 125
Liu, Y., Xiang, Y., Erdélyi, R., et al. 2018b, ApJ, 856, 17
Long, J., Shelhamer, E., & Darrell, T. 2015, in IEEE Conf. on Computer Vision and Pattern Recognition (CVPR) (Piscataway, NJ: IEEE), 3431
Mehltretter, J. P. 1974, SoPh, 38, 43
Möstl, C., Hanslmeier, A., Sobotka, M., Puschmann, K., & Muthsam, H. J. 2006, SoPh, 237, 13
Müller, H.-R., Zank, G. P., & Lipatov, A. e. S. 2000, JGR, 105, 27419
Muller, R., & Roudier, T. 1984, SoPh, 94, 33
Muller, R., Utz, D., & Hanslmeier, A. 2011, SoPh, 274, 87
Neubeck, A., & Gool, L. 2006, in 18th Int. Conf. on Pattern Recognition (ICPR'06) (Piscataway, NJ: IEEE), 850
Parker, E. N. 1988, ApJ, 330, 474
Peckover, R. S., & Weiss, N. O. 1978, MNRAS, 182, 189
Ren, S., He, K., Girshick, R. B., & Sun, J. 2015, ITPAM, 39, 1137
Requerey, I. S., Del Toro Iniesta, J. C., Bellot Rubio, L. R., et al. 2015, ApJ, 810, 79
Riethmüller, T. L., Solanki, S. K., Martínez, P. V., et al. 2010, ApJL, 723, L169
Roberts, P. H., & Soward, A. M. 1983, MNRAS, 205, 1171
Romano, P., Berrilli, F., Criscuoli, S., et al. 2012, SoPh, 280, 407
Roudier, T., Espagnet, O., Muller, R., & Vigneau, J. 1994, A&A, 287, 982
Russell, B. C., Torralba, A., Murphy, K. P., & Freeman, W. T. 2008, International Journal of Computer Vision, 77, 157
Rutten, R. J., Kiselman, D., Rouppe van der Voort, L., & Plez, B. 2001, in ASP Conf. Ser. 236, Advanced Solar Polarimetry—Theory, Observation, and Instrumentation, ed. M. Sigwarth (San Francisco, CA: ASP), 445
Sánchez Almeida, J. 2004, in ASP Conf. Ser. 325, The Solar-B Mission and the Forefront of Solar Physics, ed. T. Sakurai & T. Sekii (San Francisco, CA: ASP), 115
Sánchez Almeida, J., Bonet, J. A., Viticchié, B., & Del Moro, D. 2010, ApJL, 715, L26
Schüssler, M., Shelyag, S., Berdyugina, S., Vögler, A., & Solanki, S. K. 2003, ApJL, 597, L173
Solanki, S. K. 1993, SSRv, 63, 1
Steiner, O., Hauschildt, P. H., & Bruls, J. 2001, A&A, 372, L13
Stenflo, J. O. 1985, SoPh, 100, 189
Utz, D., Hanslmeier, A., Möstl, C., et al. 2009, A&A, 498, 289
Utz, D., Jurčák, J., Hanslmeier, A., et al. 2013, A&A, 554, A65
Vernazza, J. E., Avrett, E. H., & Loeser, R. 1981, ApJS, 45, 635
Voigtlaender, P., Krause, M., Osep, A., et al. 2019, in IEEE/CVF Conference on Computer Vision and Pattern Recognition (CVPR) (Piscataway, NJ: IEEE), 7934
Wiehr, E., Bovelet, B., & Hirzberger, J. 2004, A&A, 422, L63
Wöger, F., von der Lühe, O., & Reardon, K. 2008, A&A, 488, 375
Xiong, J., Yang, Y., Jin, C., et al. 2017, ApJ, 851, 42
Yang, Y., Ji, K., Feng, S., et al. 2015a, ApJ, 810, 88
Yang, Y., Li, X., Bai, X., et al. 2019, ApJ, 887, 129
Yang, Y.-F., Lin, J.-B., Feng, S., et al. 2014, RAA, 14, 741
Yang, Y.-F., Qu, H.-X., Ji, K.-F., et al. 2015b, RAA, 15, 569
Yurchyshyn, V. B., Goode, P. R., Abramenko, V. I., et al. 2010, ApJ, 722, 1970
Zakharov, V., Gandorfer, A., Solanki, S. K., & Löfdahl, M. 2005, A&A, 437, L43
Zhao, Y., Yu, Z., Chen, F., Zhang, J., & Yang, B. 2009, ESRv, 97, 242